The Astrophysical Journal, 959:134 (10pp), 2023 December 20 https://doi.org/10.3847/1538-4357/ad045a

Hubble Constant Measurement from Three Large-separation Quasars Strongly Lensed by Galaxy Clusters

Kate Napier[1], Keren Sharon[1], Håkon Dahle[2], Matthew Bayliss[3], Michael D. Gladders[4,9], Guillaume Mahler[5,6], Jane R. Rigby[7], and Michael Florian[8]
[1] Department of Astronomy, University of Michigan, 1085 S University Avenue, Ann Arbor, MI 48109, USA; kanapier@umich.edu
[2] Institute of Theoretical Astrophysics, University of Oslo, P.O. Box 1029, Blindern, NO-0315 Oslo, Norway
[3] Department of Physics, University of Cincinnati, Cincinnati, OH 45221, USA
[4] Department of Astronomy and Astrophysics, University of Chicago, 5640 South Ellis Avenue, Chicago, IL 60637, USA
[5] Centre for Extragalactic Astronomy, Durham University, South Road, Durham DH1 3LE, UK
[6] Institute for Computational Cosmology, Durham University, South Road, Durham DH1 3LE, UK
[7] Observational Cosmology Lab, Code 665, NASA Goddard Space Flight Center, 8800 Greenbelt Road, Greenbelt, MD 20771, USA
[8] Steward Observatory, University of Arizona, 933 North Cherry Avenue, Tucson, AZ 85721, USA
[9] Kavli Institute for Cosmological Physics, University of Chicago, 5640 South Ellis Avenue, Chicago, IL 60637, USA
Received 2023 February 8; revised 2023 September 18; accepted 2023 October 16; published 2023 December 14

Abstract

Tension between cosmic microwave background–based and distance ladder–based determinations of the Hubble constant H_0 motivates the pursuit of independent methods that are not subject to the same systematic effects. A promising alternative, proposed by Refsdal in 1964, relies on the inverse scaling of H_0 with the delay between the arrival times of at least two images of a strongly lensed variable source such as a quasar. To date, Refsdal's method has mostly been applied to quasars lensed by individual galaxies rather than by galaxy clusters. Using the three quasars strongly lensed by galaxy clusters (SDSS J1004+4112, SDSS J1029+2623, and SDSS J2222+2745) that have both multiband Hubble Space Telescope data and published time delay measurements, we derive H_0, accounting for the systematic and statistical sources of uncertainty. While a single time delay measurement does not yield a well-constrained H_0 value, analyzing the systems together tightens the constraint. Combining the six time delays measured in the three cluster-lensed quasars gives $H_0 = 74.1 \pm 8.0$ km s^{-1} Mpc^{-1}. To reach 1% uncertainty in H_0, we estimate that a sample size of order of 620 time delay measurements of similar quality as those from SDSS J1004+4112, SDSS J1029+2623, and SDSS J2222+2745 would be needed. Improving the lens modeling uncertainties by a factor of two and a half may reduce the needed sample size to 100 time delays, potentially reachable in the next decade.

Unified Astronomy Thesaurus concepts: Gravitational lensing (670); Cosmology (343); Hubble constant (758); Quasars (1319); Galaxy clusters (584)

1. Introduction

The Hubble parameter H_0, which describes the current expansion rate of the Universe, has been sought since the discovery in the 1920s that the Universe is expanding (Lemaître 1927; Hubble 1929). At the turn of the last century, measurements of H_0 started converging around $H_0 = 70$ km s^{-1} Mpc^{-1}. However, as H_0 measurements have become increasingly precise, the so-called "Hubble Tension" has arisen between the estimates from early and late-Universe probes. The Planck Collaboration reported $H_0 = 67.4 \pm 0.5$ km s^{-1} Mpc^{-1} (Planck Collaboration et al. 2020). They used density fluctuations encoded in the cosmic microwave background (CMB) at the surface of last scattering to determine H at that epoch and then used a spatially flat cosmological model to extrapolate to H_0. By contrast, the "Supernovae, H_0, for the Equation of State of Dark Energy" (SH0ES) collaboration combined Gaia parallaxes and multiband Hubble Space Telescope (HST) photometry of Milky Way Cepheids to calibrate the extragalactic distance scale and derive $H_0 = 73.04 \pm 1.04$ km s^{-1} Mpc^{-1} (Riess et al. 2022). The Planck and SH0ES values, which respectively capture the early and late-time physics of the Universe, differ by 5σ. Freedman (2021) applied an updated tip of the red giant branch (TRGB) calibration to a distant sample of Type Ia supernovae from the Carnegie Supernova Project and obtained $H_0 = 69.8 \pm 0.6$ (stat) ± 1.6 (sys) km s^{-1} Mpc^{-1}, consistent with the CMB value, and within 2σ of the SH0ES value, owing to the larger uncertainties. The discrepancy between different H_0 methods may indicate a deviation from the standard Λ cold dark matter (ΛCDM) model, and therefore new physics, or the presence of unknown or underestimated systematics. Either way, this tension remotivates the pursuit of other H_0 determination methods that are not prone to the same systematics.

An alternative H_0 determination method, proposed by Refsdal (1964), uses the fact that H_0 scales inversely with the delay between the arrival times of at least two images of a strongly lensed variable source, such as a quasar or a supernova. Due to the rarity of galaxy clusters lensing quasars or supernovae, the Refsdal H_0 technique has primarily been sought with galaxy-scale lenses (see, e.g., the recent reviews by Birrer et al. 2022; Moresco et al. 2022; Treu et al. 2022).

Of the >300 known lensed quasars, the vast majority are lensed by individual galaxies (Lemon et al. 2019, 2023). Quasars lensed by individual galaxies have been used to obtain H_0. For example, the H_0 Lenses in COSMOGRAIL's Wellspring (H0LiCOW) collaboration performed a joint analysis of six galaxy-lensed quasars to obtain $H_0 = 73.3^{+1.7}_{-1.8}$ km s^{-1} Mpc^{-1}

(Wong et al. 2020). This value is consistent with the Cepheid-calibrated measurement from the SH0ES collaboration.

The main uncertainty with galaxy-scale lenses is the mass-sheet degeneracy, which does not allow the total density profile to be precisely constrained from the lensing information alone. Kochanek (2020) argued that the H0LiCOW H_0 measurement uncertainty was underestimated due to artificially restricting the mass-sheet degeneracy through specific mass model assumptions. To account for the mass-sheet degeneracy in the uncertainty completely, Birrer et al. (2020) permitted additional freedom in the lens model and constrained the mass profile with stellar kinematics. Unsurprisingly, this led to an increase in the uncertainty level to ∼8%, but the mean H_0 value remained at ∼73 km s^{-1} Mpc^{-1}. To reduce the uncertainty, Birrer et al. (2020) included further information on the galaxy mass profile from the Sloan Lens ACS sample and obtained $H_0 = 67.4 \pm 3.7$ km s^{-1} Mpc^{-1}. Resolved JWST and Extremely Large Telescope observations of the stellar kinematics in the lens galaxies may significantly reduce these sources of systematic errors (Birrer & Treu 2021).

What has remained largely unexplored until now is determining H_0 by using quasars that are strongly lensed by galaxy clusters. For several reasons, cluster-lensed quasars can potentially overcome some of the difficulties faced by individual galaxy lenses. First, since galaxy clusters have deeper potential wells than galaxies, cluster lenses produce longer time delays of order months to years compared to typically a month in galaxy lenses. Consequently, the observationally measured time-delay values will have smaller fractional uncertainty, which then will propagate to reduced uncertainty in H_0 due to the inverse scaling of H_0 with the time delay. Second, the light curves of cluster-lensed quasars are less likely to be affected by microlensing from stars in the lens plane, because the mass distribution is dominated by dark matter at the projected radius at which the images appear. Third, galaxy cluster mass distributions are less affected by complex baryonic physics than those of galaxy lenses; the complex baryonic surface density of galaxy-scale lenses may be a significant source of systematic uncertainty. Cluster-scale lenses are less affected by the mass-sheet degeneracy due to having multiple images of lensed sources from various source-plane redshifts behind the lens (Grillo et al. 2020). A challenge that must be contended with, however, is the complexity of cluster lenses.

Two inputs are necessary to use cluster-lensed quasars to determine H_0. The first is an observational measurement of the time delay between the multiple quasar images, and the second is an accurate mapping of the projected density of the dark and luminous mass at the cluster core. High-accuracy lens models require space-based resolution and spectroscopic follow-up. Of the seven published cluster-lensed quasars to date (Inada et al. 2003, 2006; Dahle et al. 2013; Shu et al. 2018, 2019; Martinez et al. 2023; Napier et al. 2023), only three have the necessary data available to determine H_0: SDSS J1004+4112, SDSS J1029+2623, and SDSS J2222+2745. In this paper, we use the available archival HST data and the latest measurements of time delays and spectroscopic redshifts of background sources from the literature to obtain an independent measurement of H_0 from these three systems.

This paper is organized as follows: in Section 2, we outline the theory of observational gravitational lensing time delay and its dependence on H_0. In Section 3 we detail the lens modeling procedure. In Sections 4–6, we give an overview of the three cluster-lensed quasar systems used in this H_0 analysis and provide details about their HST and spectroscopic data, time delays, and lens models. In Section 7, we present our constraints on H_0. We conclude in Section 8 with a discussion of our H_0 result and the future prospects of the time-delay H_0 method.

Throughout the paper, we adopt the standard ΛCDM flat cosmological model with $\Omega_m = 0.3$ and $\Omega_\Lambda = 0.7$.

2. Time-delay Analysis

The Refsdal H_0 method is possible due to the measurable delay between the arrival time of two or more images of a variable source such as a quasar. Under the thin lens approximation, a packet of light that travels from the source to the observer will be delayed by time t given by the arrival time surface (Schneider 1985):

$$t(\boldsymbol{\theta}, \boldsymbol{\beta}) = \frac{1 + z_l}{c} \frac{d_l d_s}{d_{ls}} \left[\frac{1}{2} (\boldsymbol{\theta} - \boldsymbol{\beta})^2 - \psi(\boldsymbol{\theta}) \right], \tag{1}$$

where z_l is the redshift of the lens; d_l, d_s, and d_{ls} are the angular diameter distances from the observer to the lens, to the source, and between the lens and the source, respectively; $\boldsymbol{\theta}$ is the image position in the image plane; $\boldsymbol{\beta}$ is the unobserved source position; and $\psi(\boldsymbol{\theta})$ is the gravitational lensing potential. The arrival time t is a combination of the path length and the gravitational time delay ($t = t_{\rm geometric} + t_{\rm grav}$). The last term, $\tau(\theta; \beta) = \left[\frac{1}{2} (\boldsymbol{\theta} - \boldsymbol{\beta})^2 - \psi(\boldsymbol{\theta}) \right]$, is also known as the Fermat potential. The multiple images of a strongly lensed source appear in the stationary points of the arrival time surface, that is, in the minima, maxima, and saddle points. H_0 is incorporated in Equation (1) because of its inverse scaling with the angular diameter distances:

$$d_A(z_1, z_2) = \frac{1}{(1 + z_2)} \frac{c}{H_0} \int_{z_1}^{z_2} \frac{dz}{E(z; \Omega_m, \Omega_\Lambda)}, \tag{2}$$

for flat cosmology, where $E(z; \Omega_m, \Omega_\Lambda)$ is a dimensionless function given by $E(z; \Omega_m, \Omega_\Lambda) = \sqrt{\Omega_m (1 + z)^3 + \Omega_\Lambda}$. The matter density and vacuum energy density parameters are Ω_m and Ω_Λ, respectively. Conveniently, H_0 is disentangled from the other cosmological parameters in the angular diameter distance equation (Equation (2)). After substituting Equation (2) into $d_l d_s / d_{ls}$ in Equation (1), the time delay is determined by applying Equation (1) for two image positions corresponding to the same source position and taking the difference. The time delay between the images thus becomes:

$$\Delta t = \left(\frac{1}{H_0} \right) \left(\frac{\int_0^{z_l} \frac{dz}{E(z)} \int_0^{z_s} \frac{dz}{E(z)}}{\int_{z_l}^{z_s} \frac{dz}{E(z)}} \right) \times \left(\frac{1}{2} [(\boldsymbol{\theta}_1 - \boldsymbol{\beta})^2 - (\boldsymbol{\theta}_2 - \boldsymbol{\beta})^2] - [\psi(\boldsymbol{\theta}_1) - \psi(\boldsymbol{\theta}_2)] \right). \tag{3}$$

The first term on the right-hand side of the time-delay equation gives the Hubble parameter; the second term contains the dependence on cosmological parameters other than H_0; and the third term is solved by the strong gravitational lens model.

We neglect the higher-order effects of the cosmological parameters and fix the second term on the right-hand side in Equation (3) using the fiducial cosmology. The left-hand side of the equation is the measurement of the time delay, e.g., from monitoring and comparing the observed light curves of two images of the variable source.

Once we compute a model of the lensing mass distribution (see Section 3), we determine the model-predicted excess arrival time surface (Equation (3)) with respect to one of the quasar images. Assuming our lens model is a correct description of the matter distribution, we then leverage the fact that the time delay scales inversely with H_0. We compare the model-predicted time delays between images to the observational measurements of the time delays to obtain H_0 via:

$$H_0 = H_{0,\mathrm{model}} \times \frac{\Delta t_{\mathrm{model}}}{\Delta t_{\mathrm{measured}}}, \quad (4)$$

where $H_{0,\mathrm{model}}$ is the H_0 value used to generate the Fermat potential from the lensing analysis (we assumed $H_{0,\mathrm{model}} = 70$ km s^{-1} Mpc^{-1}), $\Delta t_{\mathrm{model}}$ is the model-predicted time delay between the quasar images, and $\Delta t_{\mathrm{measured}}$ is the observational measurement of the time delay between the pair of quasar images.

3. Lens Modeling

We computed the lens models with the publicly available software `Lenstool` (Jullo et al. 2007). `Lenstool` is a "parametric" modeling algorithm that describes the lensing mass distribution as a linear combination of galaxy-scale, group-scale, and cluster-scale halos, each of which is parameterized as a pseudo-isothermal ellipsoidal mass distribution (PIEMD, also called dPIE; Elíasdóttir et al. 2007). The three-dimensional density distribution of the PIEMD is:

$$\rho(r) = \frac{\rho_0}{(1 + r^2/r_c^2)(1 + r^2/r_{\mathrm{cut}}^2)}, \quad (5)$$

which has seven parameters whose values can either be fixed or varied: position (x, y); ellipticity $e = (a^2 - b^2)/(a^2 + b^2)$, where a and b are the semimajor and semiminor axes, respectively; position angle θ; core radius r_c; truncation radius r_{cut}; and effective velocity dispersion σ_0. The parameters of the group-scale and cluster-scale halos are typically allowed to vary. The exception is r_{cut} for the cluster-scale halos as this radius usually occurs outside the region where strong lensing evidence is found, and thus, cannot be constrained.

`Lenstool` uses a Markov Chain Monte Carlo (MCMC) sampling of parameter space. The best-fit model is identified as the one that minimizes the scatter between the model-predicted and observed image locations in the image plane ("image-plane minimization") or minimizes the scatter between the predicted source locations of multiple images in the source plane ("source-plane minimization"). The lens models employ the strong lensing information of multiple imaged galaxies (arcs), whose positions and redshifts are used as model constraints. The availability of lensing constraints strongly affects the accuracy of lens models, as they are used as local solutions of the lensing equations and constrain the projected mass density distribution at the cluster's core. The mass distribution and magnification are sensitive to the accurate identifications and positions of multiply images and to the redshifts of the lensed galaxies. It is necessary to include a few spectroscopic redshifts in the lens model to avoid incorrect results (Johnson & Sharon 2016). As described in more detail in the following sections, all of the multiply imaged galaxies used as constraints in the lens models for SDSS J1004+4112, SDSS J1029+2623, and SDSS J2222+2745 were robustly determined; hence the image identifications are not a significant source of systematic uncertainty.

To select cluster-member galaxies, we followed the procedure of Gladders & Yee (2000), by selecting galaxies that fall on the cluster red sequence in a color–magnitude diagram. For SDSS J1029+2623 we also incorporated spectroscopic redshift information (see Section 5). The galaxy-scale halos' positional parameters (x, y, e, and θ) are measured with `Source Extractor` (Bertin & Arnouts 1996) and fixed. The r_c, r_{cut}, and σ_0 of the galaxy-scale halos are scaled to their observed luminosity following the scaling relations in Limousin et al. (2005). A potential misidentification of cluster-member galaxies is unlikely to be a significant source of systematic uncertainty. For example, Napier et al. (2023) found that excluding a subsample of cluster members from the lens model did not significantly change the predicted time delays.

4. SDSS J1004+4112

SDSS J1004+4112 was the first discovered galaxy cluster strongly lensing a quasar (Inada et al. 2003). The cluster at $z = 0.68$ strongly lenses a quasar at $z = 1.734$ into five images, with a maximum image separation of 14.″6 (Table 1). The cluster also strongly lenses several background sources at $z = 2.74$ (Sharon et al. 2005), $z = 3.288$ (Sharon 2008; Oguri 2010), and $z = 3.332$ (Sharon et al. 2005; Table 2).

We used archival HST multicolor imaging from the Advanced Camera for Surveys (ACS). The SDSS J1004+4112 imaging data include GO-10509 (PI: Kochanek) ACS/F814W, F555W, and F435W (10 orbits); GO-9744 (PI: Kochanek) ACS/F814W and F555W (two orbits); and GO-10793 (PI: Gal-Yam) ACS/F814W (one orbit). These data were originally proposed to identify multiply imaged galaxies to construct a mass model (Sharon et al. 2005), search for the fifth quasar image (Inada et al. 2005), derive Ω_Λ, perform a weak lensing analysis, and search for supernovae in massive high-redshift clusters (Sharon et al. 2010). These data also enabled studies of the spectral energy distribution of the quasar host galaxy (Ross et al. 2009), the ultraviolet upturn in red sequence galaxies (Ali et al. 2018), and active galactic nuclei in massive clusters (Klesman & Sarajedini 2012).

We modeled SDSS J1004+4112 using one cluster-scale halo, one brightest cluster galaxy (BCG)-scale halo, and a galaxy-scale halo for each of the cluster-member galaxies, 168 in total, five (including the BCG) of which have their slope parameters optimized instead of adopting the scaling relations from Limousin et al. (2005). We optimized the parameters for these five galaxies because of either their proximity to the quasar images or their necessity for reproducing the lensed image configuration.

We modeled the cluster using both source-plane minimization and image-plane minimization, and evaluated the quality of the models obtained by each approach. While formally the image-plane minimization resulted in a better image-plane scatter, these models produced additional quasar images that are not observed. Therefore, we proceeded with the source-plane minimization for SDSS J1004+4112 for the remainder of

Table 1
The Quasar Image Positions and Redshifts

Target	QSO Image	QSO z	R.A. [J2000]	Decl. [J2000]	μ
SDSS J1004+4112					
	A	1.734	151.1450074	41.2109193	23.3 ± 7.2
	B	1.734	151.1454888	41.2119003	13.8 ± 3.8
	C	1.734	151.1409266	41.2096668	10.7 ± 1.3
	D	1.734	151.1419060	41.2136092	4.7 ± 1.1
	E	1.734	151.1423413	41.2122017	0.2 ± 0.05
SDSS J1029+2623					
	A	2.1992	157.3081009	26.3883044	5.5 ± 0.3
	B	2.1992	157.3093619	26.3944624	20.8 ± 3.9
	C	2.1992	157.3095755	26.3939894	8.0 ± 8.0
SDSS J2222+2745					
	A	2.805	335.537707	27.760543	12.0 ± 5.0
	B	2.805	335.536690	27.761119	8.4 ± 5.0
	C	2.805	335.532960	27.760505	5.5 ± 2.0
	D	2.805	335.536205	27.758901	0.9 ± 0.5
	E	2.805	335.536007	27.758248	0.6 ± 0.2
	F	2.805	335.535874	27.759723	0.7 ± 0.4

Note. Also included are the model-predicted median magnifications at the observed positions of the quasar images.

the analysis. We note that the best-fit lens model produced large scatter between the observed and model-predicted positions in the image plane for quasar image C. In our results, we checked what happens when image C is removed from the H_0 measurement.

The model consists of 27 free parameters and 78 constraints. The HST data and the lens model for SDSS J1004+4112 are shown in Figure 1. The redshifts of the arcs in our lens model are the same as those used by Forés-Toribio et al. (2022). The strong lensing mass model parameters are reported in Table 3.

The measured time delay between images A and B ($\Delta t_{\rm AB} = -38.4 \pm 2.0$ days) was first published in Fohlmeister et al. (2007). In this notation, a positive value of the time delay means image A leads the other image. In addition to reporting a refined value of $\Delta t_{\rm AB} = -40.6 \pm 1.8$ days, Fohlmeister et al. (2008) measured the time delay between images A and C ($\Delta t_{\rm AC} = -821.6 \pm 2.1$ days) and set a lower limit of $\Delta t_{\rm AD} > 1250$ days. After the completion of a 14.5 yr monitoring campaign at the 1.2 m Fred Lawrence Whipple Observatory (FLWO), Muñoz et al. (2022) presented new light curves for the four brightest images in SDSS J1004+4112, resulting in updated time-delay values of $\Delta t_{\rm AB} = -43.01 \pm 0.27$ days, $\Delta t_{\rm AC} = -825.23 \pm 0.46$ days, and $\Delta t_{\rm AD} = 1633.23 \pm 0.97$ days.

5. SDSS J1029+2623

SDSS J1029+2623 is a cluster at $z = 0.588$ that is strongly lensing a quasar at $z = 2.1992$ into three images (Inada et al. 2006; Oguri et al. 2008; Table 1). The quasar images are in a naked cusp configuration with a maximum image separation of $22\farcs5$.

Acebron et al. (2022) reported spectroscopic redshifts of several galaxies in the field, based on Multi Unit Spectroscopic Explorer (MUSE) spectroscopy from the Very Large Telescope. They refined the redshift measurement of the quasar to $z = 2.1992$ (formerly reported as $z = 2.197$; Inada et al. 2006). The other spectroscopically confirmed objects from MUSE include a doubly imaged galaxy at $z = 2.1812$, a septuply imaged galaxy at $z = 3.0275$, a quadruply imaged galaxy at $z = 3.0278$, a doubly imaged galaxy at $z = 1.0232$, and a quadruply imaged galaxy at $z = 5.0622$ (Acebron et al. 2022; Table 2).

We used archival HST multicolor imaging from GO-12195 (PI: Oguri): WFC3/F160W (two orbits), ACS/F814W (three orbits), and ACS/F475W (two orbits). These data were originally proposed to identify multiply imaged galaxies to construct a mass model that could be used to understand the anomalous flux ratios between two of the quasar images and the dynamical state of the cluster better (Oguri et al. 2013). These HST data also enabled a weak lensing analysis and a morphology study of the quasar host galaxy (Oguri et al. 2013).

Our lens model, which builds on the results from Acebron et al. (2022) and Oguri et al. (2013), contains 48 constraints and 33 free parameters. All of the model constraints are taken from Acebron et al. (2022). The model includes two cluster-scale dark matter halos that were allowed to vary in position around the two BCGs as well as two galaxy-scale halos that were fixed to the BCGs' positions. Additionally, a foreground galaxy ($z = 0.5111$ from MUSE) and a background galaxy ($z = 0.6735$ from MUSE) along the line of sight are both modeled at the cluster redshift since `Lenstool` does not yet implement a multiplane lensing framework. This approach improves the accuracy of the lensing analysis outputs compared to omitting these interlopers from the model (Raney et al. 2020). The lens model includes 204 galaxy-scale halos.

Our lens model differs from Acebron et al. (2022) in the following ways. Whereas Acebron et al. (2022) include a model (Model 1) with an external shear component, we opted to not include this component as its inclusion does not significantly improve the rms scatter in the source plane. Additionally, for consistency with the other clusters modeled in this paper, our galaxy-scale halos have ellipticities, whereas Acebron et al. (2022) use spherical halos. We constructed our galaxy catalog as described in Section 3, taking into account the MUSE spectroscopy to determine the red sequence (see Sharon et al. 2023). We used the ACS F814W versus F475W for selection. We identified the red sequence by fitting a line to the spectroscopic members in this phase space, with four iterations of sigma clipping.

Table 2
Positions and Spectroscopic Redshifts of the Multiply Imaged Background Sources Used as Constraints in the Strong Lens Models for SDSS J1004+4112 and SDSS J1029+2623

System	ID	R.A. [J2000]	Decl. [J2000]	z
SDSS J1004+4112				
	QSO-A	151.1450074	41.2109193	1.734
	QSO-B	151.1454888	41.2119003	1.734
	QSO-C	151.1409266	41.2096668	1.734
	QSO-D	151.1419060	41.2136092	1.734
	QSO-E	151.1423413	41.2122017	1.734
	2.1	151.1418821	41.2102917	2.74
	2.2	151.1468800	41.2153908	2.74
	21.1	151.1417325	41.2103272	2.74
	21.2	151.1470383	41.2153011	2.74
	21.3	151.1419526	41.2116044	2.74
	22.1	151.1416225	41.2103033	2.74
	22.2	151.1471250	41.2152436	2.74
	3.1	151.1414121	41.2099250	3.288
	3.2	151.1476847	41.2152121	3.288
	31.1	151.1413250	41.2099825	3.288
	31.2	151.1477393	41.2151976	3.288
	32.1	151.1412104	41.2100544	3.288
	32.2	151.1478065	41.2151979	3.288
	33.1	151.1411279	41.2101547	3.288
	33.2	151.1478809	41.2151884	3.288
	33.3	151.1418864	41.2116948	3.288
	4.1	151.1439081	41.2165866	3.332
	4.2	151.1382517	41.2153846	3.332
	4.3	151.1379048	41.2149959	3.332
	4.4	151.1434099	41.2103752	3.332
	41.1	151.1441118	41.2165193	3.332
	41.2	151.1383309	41.2153297	3.332
	41.3	151.1378932	41.2148820	3.332
	41.4	151.1434562	41.2102573	3.332
	42.1	151.1444522	41.2163884	3.332
	42.2	151.1383940	41.2153469	3.332
	42.3	151.1378407	41.2148091	3.332
	42.4	151.1434818	41.2101761	3.332
	43.1	151.1445319	41.2162919	3.332
	43.2	151.1384506	41.2154232	3.332
	43.3	151.1376594	41.2145747	3.332
	43.4	151.1435603	41.2101349	3.332
	43.5	151.1424833	41.2118271	3.332
SDSS J1029+2623				
	QSO-A	157.3081009	26.38830445	2.1992
	QSO-B	157.3093619	26.39446237	2.1992
	QSO-C	157.3095755	26.3939894	2.1992
	1.1	157.2980611	26.3907404	⋯
	1.2	157.2978817	26.3924467	⋯
	1.3	157.3008758	26.3974054	⋯
	2.1	157.2981743	26.3915325	2.1812
	2.3	157.3014749	26.3977063	2.1812
	3.1	157.2990642	26.3923892	3.0275
	3.2	157.3074114	26.3913469	3.0275
	3.3	157.3041512	26.3982630	3.0275
	3.4	157.3015481	26.3880193	3.0275
	3.5	157.3017377	26.3879213	3.0275
	3.6	157.3018385	26.3878900	3.0275
	3.7	157.3032208	26.3919632	3.0275
	4.1	157.2992278	26.3925219	3.0278
	4.2	157.3076382	26.3913247	3.0278
	4.3	157.3043869	26.3981437	3.0278
	4.4	157.3023985	26.3877048	3.0278
	4.5	157.3035100	26.3920169	3.0278
	5.1	157.3019777	26.3946563	1.0232
	5.3	157.3008781	26.3917377	1.0232
	7.1	157.3075794	26.3951262	5.0622
	7.2	157.3064130	26.3960500	5.0622
	7.3	157.3014210	26.3936610	5.0622
	7.4	157.3012420	26.3938020	5.0622

Note. See Table 1 from Sharon et al. (2017) for the lensing constraints for SDSS J2222+2745.

We found that the source-plane minimization did a better job at predicting the quasar image positions in this cluster than the image-plane minimization, possibly due to the close proximity of quasar images B and C. Once a best-fit model was obtained, we examined the posterior distribution of image predictions and rejected from the MCMC sampling steps that did not produce this lensing configuration, i.e., not producing two separate images for A and B on either side of the critical curve. Since these two images lie very close to the critical curve, some parameter combinations produce solutions in which these two images merge and only image A of the quasar remains, in contrast to the observed lensing evidence.

The HST data and the lens model for SDSS J1029+2623 are shown in Figure 1. The strong lensing mass model parameters are reported in Table 4.

Fohlmeister et al. (2013) published a time-delay measurement between images A and B ($\Delta t_{\rm AB} = 744 \pm 10$ days) based on photometric monitoring campaign at the FLWO 1.2 m.

6. SDSS J2222+2745

SDSS J2222+2745, discovered by Dahle et al. (2013), is a cluster at $z = 0.49$ that strongly lenses a quasar at $z = 2.805$ (Table 1). The quasar is imaged six times (Sharon et al. 2017) with a maximum image separation of $15\farcs1$.

Spectroscopy of other lensed galaxies was obtained by the Gemini North Telescope. These data include triply imaged and doubly imaged knots from a galaxy at $z = 4.562$ and a doubly imaged galaxy at $z = 2.2963$ (Sharon et al. 2017).

We used archival HST multicolor imaging from GO-13337 (PI: Sharon): WFC3/F160W and F110W (one orbit) and ACS/F814W, F606W, and F435W (six orbits). These data were originally proposed to detect any additional quasar images and to compute a mass model (Sharon et al. 2017). Additionally, these HST data have enabled a spatially resolved study of the Lyα emission in the quasar host galaxy (Bayliss et al. 2017).

We adopted the lens model from Sharon et al. (2017) with 32 constraints and 31 free parameters. SDSS J2222+2745 is modeled using image-plane minimization with one cluster-scale halo and 172 galaxy-scale halos. Sharon et al. (2017) included as constraints triply imaged and doubly imaged knots at the quasar's redshift of $z = 2.805$, and triply imaged and doubly imaged knots from a galaxy at $z = 4.562$. Two separate triply imaged galaxies had their redshifts left as free parameters, with priors of $2.0 \leqslant z \leqslant 4.0$ and $3.8 \leqslant z \leqslant 5.0$, respectively, based on a photometric redshift analysis. The HST data and the lens model for SDSS J2222+2745 are shown in Figure 1. Table 3 of Sharon et al. (2017) lists the strong lensing mass model parameters.

Dahle et al. (2015) first published time-delay measurements between images A and B ($\Delta t_{\rm AB} = 47.7 \pm 6.0$ days) and A and C ($\Delta t_{\rm AC} = -722 \pm 24$ days). Then Dyrland (2019) reported updated values for the time delays between images A and B ($\Delta t_{\rm AB} = 42.44\ ^{+1.36}_{-1.44}$ days) and images A and C

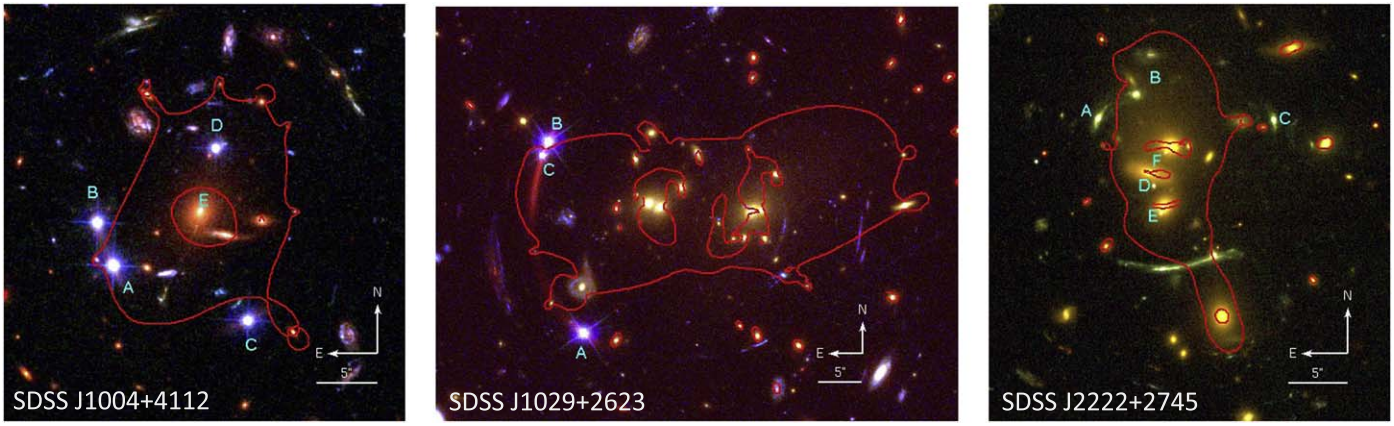

Figure 1. HST imaging of the three cluster-lensed quasars used to derive H_0. We computed the lens models for SDSS J1004+4112 and SDSS J1029+2623. SDSS J2222+2745 is reproduced from Sharon et al. (2017). The positions of the quasar images are denoted with the cyan letters. The critical curves, the loci of maximum magnification at a specified source redshift, are generated at the quasar redshifts—$z = 1.734$, $z = 2.1992$, and $z = 2.805$, for SDSS J1004+4112, SDSS J1029+2623, and SDSS J2222+2745, respectively, and are plotted in red.

Table 3
Strong Lensing Mass Model Parameters for SDSS J1004+4112

Component No.	ΔR.A. (arcsec)	Δdecl. (arcsec)	e	θ (deg)	σ_0 (km s^{-1})	$r_{\rm cut}$ (kpc)	r_c (kpc)
1	$0.085^{+0.52}_{-2.56}$	$3.07^{+5.83}_{-1.30}$	$0.17^{+0.022}_{-0.030}$	$66.39^{+3.70}_{-3.22}$	987^{+245}_{-84}	[1500]	$126.27^{+112.43}_{-33.97}$
2	[0]	[0]	[0.40]	$63.98^{+4.34}_{-5.31}$	461^{+48}_{-52}	$181.42^{+13.77}_{-28.04}$	$5.65^{+0.99}_{-1.62}$
3	[−1.963]	[−1.832]	$0.42^{+0.25}_{-0.19}$	[349.480]	235^{+10}_{-14}	$30.30^{+7.045}_{-12.29}$	$2.68^{+0.99}_{-0.68}$
4	[−7.659]	[−9.821]	$0.43^{+0.22}_{-0.29}$	[131.13]	127^{+33}_{-29}	$20.13^{+6.64}_{-8.33}$	$1.62^{+1.48}_{-1.06}$
5	[8.463]	[−3.877]	$0.44^{+0.24}_{-0.27}$	[133.89]	114^{+31}_{-28}	$13.28^{+2.97}_{-2.97}$	$2.26^{+0.92}_{-1.20}$
6	[−11.220]	[11.401]	$0.42^{+0.29}_{-0.29}$	$150.24^{+22.22}_{-34.44}$	76^{+9}_{-7}	$22.46^{+5.79}_{-6.85}$	$3.18^{+0.85}_{-0.85}$

Note. Median values and the 1σ confidence level from the MCMC are reported. The coordinates ΔR.A. and Δdecl. are listed in arcseconds measured east and north from the core of component No. 2 at [R.A., decl.] = [151.142381, 41.212131]. The other parameters are the ellipticity e, the position angle θ, the velocity dispersion σ_0, the cut radius $r_{\rm cut}$, and the core radius r_c. The position angle θ is measured north of west. In converting from angular units to kiloparsecs, an H_0 value of 70 km s^{-1} Mpc^{-1} was used. The parameters listed in square brackets were not optimized.

Table 4
Strong Lensing Mass Model Parameters for SDSS J1029+2623

Component No.	ΔR.A. (arcsec)	Δdecl. (arcsec)	e	θ (deg)	σ_0 (km s^{-1})	$r_{\rm cut}$ (kpc)	r_c (kpc)
1	$10.01^{+0.62}_{-0.53}$	$0.71^{+0.25}_{-0.23}$	$0.53^{+0.031}_{-0.034}$	$172.80^{+2.24}_{-2.27}$	650^{+21}_{-20}	[1500]	$31.39^{+4.37}_{-3.78}$
2	$-3.04^{+1.38}_{-1.16}$	$3.62^{+0.46}_{-0.58}$	$0.55^{+0.052}_{-0.055}$	$17.25^{+4.87}_{-5.10}$	528^{+30}_{-20}	[1500]	$37.95^{+6.42}_{-6.62}$
3	$-2.48^{+1.25}_{-1.35}$	$-0.11^{+1.83}_{-2.35}$	$0.61^{+0.10}_{-0.062}$	$45.57^{+7.24}_{-9.24}$	385^{+43}_{-52}	[1500]	$57.82^{+9.47}_{-11.86}$
4	[−3.808]	[−1.354]	$0.51^{+0.19}_{-0.21}$	$69.07^{+19.26}_{-15.61}$	202^{+20}_{-19}	$33.64^{+7.88}_{-6.82}$	$1.92^{+0.52}_{-0.86}$
5	[19.7]	[−8.8]	[0.0]	[0.0]	169^{+30}_{-24}	$89.94^{+19.27}_{-19.47}$	[0.0]
6	$23.87^{+0.11}_{-0.13}$	$6.50^{+0.14}_{-0.12}$	$0.30^{+0.29}_{-0.20}$	$52.06^{+26.58}_{-38.88}$	64^{+7}_{-5}	$32.65^{+11.13}_{-16.82}$	$0.51^{+0.30}_{-0.31}$

Note. Median values and the 1σ confidence level from the MCMC are reported. The coordinates ΔR.A. and Δdecl. are listed in arcseconds measured east and north from [R.A., decl.] = [157.302047, 26.392209]. The other parameters are the ellipticity e, the position angle θ, the velocity dispersion σ_0, the cut radius $r_{\rm cut}$, and the core radius r_c. The position angle θ is measured north of west. In converting from angular units to kiloparsecs, an H_0 value of 70 km s^{-1} Mpc^{-1} was used. The parameters listed in square brackets were not optimized.

($\Delta t_{\rm AC} = -696.65\ ^{+2.00}_{-2.10}$ days). These measurements were based on data from a monitoring campaign at the 2.5 m Nordic Optical Telescope.

The best-fitting statistics for the SDSS J1004+4112, SDSS J1029+2623, and SDSS J2222+2745 lens models are found in Table 5. In the analysis that follows, we used the most up-to-date time-delay values for all three systems, which are listed in Table 6.

Table 5
The Minimum χ^2, Degrees of Freedom (dof), and rms Scatter in the Source Plane

Model	χ^2	dof	rms (arcseconds)
SDSS J1004+4112	16.16	51	0.119
SDSS J1029+2623	25.44	15	0.132
SDSS J2222+2745	8.18	1	0.08

7. Results

Using the outputs of the lens models described in the previous sections, we computed the model-predicted time-delay values for each of the quasar images in each cluster field with respect to image A of the quasar (Equation (3) and Table 7).

Table 6
The Three Large-separation Lensed QSOs in the HST Archive

Target Name	z Cluster	z QSO	No. QSO Images	Widest Separation (arcsec)	No. of Lensed Sources	No. of Spec-zs	Time Delay (days)	References
SDSS J1004+4112	0.68	1.734	5	14.6	4	4	$\Delta t_{AB} = -43.01 \pm 0.27$ $\Delta t_{AC} = -825.23 \pm 0.46$ $\Delta t_{AD} = 1633.23 \pm 0.97$	Muñoz+(2022)
SDSS J1029+2623	0.58	2.1992	3	22.5	7	6	$\Delta t_{AB} = 744 \pm 10$	Fohlmeister+(2013)
SDSS J2222+2745	0.49	2.805	6	15.1	5	3	$\Delta t_{AB} = 42.44^{+1.36}_{-1.44}$ $\Delta t_{AC} = -696.65^{+2.00}_{-2.10}$	Dyrland (2019)

Note. The listed time delays are the most up-to-date values from the literature. See Fohlmeister et al. (2008) and Dahle et al. (2015) for previous measurements for SDSS J1004+4112 and SDSS J2222+2745, respectively.

Table 7
Predicted Time Delay (in Days) from the "Best" Lens Model for Each Cluster

System	Δt_{AB}	Δt_{AC}	Δt_{AD}	Δt_{AE}	Δt_{AF}
SDSS J1004+4112	−11	−783	1294	1776	N/A
SDSS J1029+2623	1060	1054	N/A	N/A	N/A
SDSS J2222+2745	54	−693	485	564	431

Note. The values are measured at the model-predicted locations of the quasar images, assuming $H_0 = 70$ km s^{-1} Mpc^{-1}.

The time delay is a sensitive function of the positions of the source ($\boldsymbol{\beta}$) and its multiple images ($\boldsymbol{\theta}_1$, $\boldsymbol{\theta}_2$). The unobservable source position and the locations of its multiple images are strongly coupled to the time delay, since stationary points in the arrival time surface determine the image-plane positions of multiple images of any given source-plane position (see Section 2). It is therefore important to measure time delays self-consistently, by obtaining the time delay at the image positions predicted by the same lensing potential. Lens models are never perfect, and small scatter between the observed and predicted positions is expected. To maintain this self-consistency, we calculated the source position $\boldsymbol{\beta}$ by ray tracing the observed position of image A ($\boldsymbol{\theta}_A$) through the lens equation, and used the same lens model to predict the image-plane positions of its counterimages ($\boldsymbol{\theta}_2$, $\boldsymbol{\theta}_3$,…). The time delay was then calculated from these predicted positions, rather than the observed positions, which may be slightly shifted from the stationary points in the Fermat potential. The scatter in the image or source plane contributes to the error budget through the MCMC exploration of the parameter space. An alternative approach to determining the source position is averaging the predicted source locations from all the quasar images, and calculating the predicted image locations of the average source. We found that this alternative approach of determining the source position produced an H_0 value consistent with the method described above, and hence, the choice of one approach versus the other is not a significant source of systematic uncertainty. In what follows, we describe the results using the former method.

Using Equation (4), we computed the H_0 value corresponding to each independent published time-delay value and corresponding predicted time delays. To generate the 1σ uncertainties in H_0, we used 500 random models from the MCMC sampling of the parameter space for each cluster to ensure smooth sampling of the H_0 posteriors.

The number of measured time delays in each field determines the number of H_0 measurements derived from each cluster: three from SDSS J1004+4112, one from SDSS J1029+2623, and two from SDSS J2222+2745, for a total of six H_0 measurements. Table 8 lists the derived H_0 values and uncertainties, obtained for the "best" lens model, i.e., the one producing the smallest scatter, and for the full posterior distribution. We find that the fractional uncertainty on H_0 calculated using the lensing analysis is consistent with the analytical propagation of errors due to the source-plane uncertainty, following Birrer & Treu (2019)'s Equation (16) and the examples therein, giving $\delta H_0(\delta\theta)/H_0 = 15\%$–$50\%$.

The resulting H_0 measurement from each quasar pair has large uncertainties due to the complexity of the lens and systematic uncertainties in the lens modeling process. Grillo et al. (2020) found that systematic effects such as adding a constant mass sheet at the cluster redshift and using a power-law profile for the mass density of the cluster's primary halo did not introduce a significant bias on the inferred H_0 value and that the statistical uncertainties dominate the total error budget. Given that SDSS J1004+4112, SDSS J1029+2623, and SDSS J2222+2745 reside in the same Universe, they all must have the same H_0; we can leverage these three independent lines of sight, with six time delays, to obtain a tighter constraint than what is possible from a single time delay, and marginalize over systematics related to line-of-sight effects such as intervening structure. We combine the results from the six time delays by taking the inverse-variance weighted mean of the six H_0 measurements, sampled from their posterior distributions. We accounted for the correlations between measurements made in the same cluster lens by using the same model realization from the MCMC to generate a linked set of H_0 values. For example, since SDSS J1004+4112 has three measured time delays, the same model realization was used to calculate the H_0 values from Δt_{AB}, Δt_{AC}, and Δt_{AD}.

Table 8
H_0 Constraints from the Time-delay Measurements in SDSS J1004+4112, SDSS J1029+2623, and SDSS J2222+2745

System	H_0 (km s^{-1} Mpc^{-1}) (From Best Model)	H_0 (km s^{-1} Mpc^{-1}) (Mean $\pm$ 1σ)
SDSS J1004+4112		
AB	17.4	56.1 ± 60.2
AC	66.4	56.3 ± 19.1
AD	55.5	70.4 ± 11.4
SDSS J1029+2623		
AB	99.7	97.0 ± 42.4
SDSS J2222+2745		
AB	89.8	104.9 ± 19.1
AC	69.3	70.3 ± 17.4

Note. The middle column is the H_0 value from the "best" lens model for each cluster. The right column lists the mean and 1σ from the Gaussian distribution fit to the H_0 values determined from 500 random models drawn from the MCMC.

We note that the observational time-delay measurement uncertainties are negligible compared to the lens modeling uncertainties. The inverse-variance weighted mean and the standard error of the weighted mean of H_0 is 74.1 ± 8.0 km s^{-1} Mpc^{-1} (Figure 2). Combining the H_0 values derived from multiple time-delay values improves the constraints on H_0, decreasing the uncertainty from ∼41% for an individual H_0 measurement to 11% for the sample. If SDSS J1004+4112's quasar image C is excluded from the analysis (see Section 4), we obtain $H_0 = 77.4 \pm 9.9$ km s^{-1} Mpc^{-1}. This value is consistent with the H_0 measurement calculated with all six time delays.

8. Discussion

Our analysis provides an independent H_0 measurement that is not sensitive to the same systematics as other methods. Our H_0 measurement, 74.1 ± 8.0 km s^{-1} Mpc^{-1} (or $H_0 = 77.4 \pm 9.9$ km s^{-1} Mpc^{-1} if excluding SDSS J1004+4112 AC), is higher than the values from CMB (67.4 ± 0.5 km s^{-1} Mpc^{-1}; Planck Collaboration et al. 2020), TRGB (69.8 ± 0.6 (stat) $\pm$ 1.6 (sys) km s^{-1} Mpc^{-1}; Freedman 2021), and Cepheids (73.04 ± 1.04 km s^{-1} Mpc^{-1}; Riess et al. 2022). However, given our measurement's larger fractional uncertainty, our H_0 value is consistent with all three.

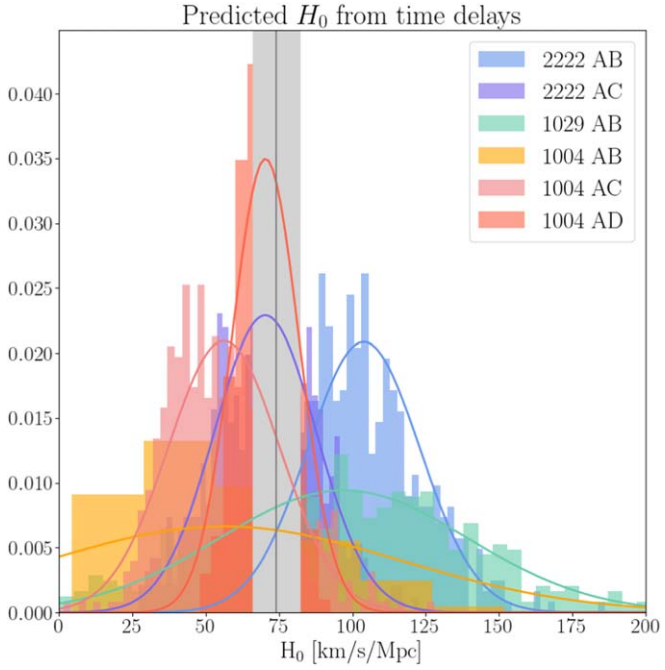

Figure 2. Constraints on H_0 from three cluster-lensed quasars, SDSS J1004+4112, SDSS J1029+2623, and SDSS J2222+2745. The histograms are created from 500 random models sampled from the MCMC. Overplotted are Gaussian fits to the distributions. Whereas individual time-delay measurements produce H_0 values with an average of 41% error, the error is decreased to 11% when the systems are analyzed together. The inverse-variance weighted mean of H_0 is 74.1 km s^{-1} Mpc^{-1} (solid gray line) and the standard error of the weighted mean is 8.0 km s^{-1} Mpc^{-1}.

Increasing the number of systems used for a combined time-delay measurement of H_0 will improve this method's competitiveness with CMB-based and distance ladder–based methods. Although four other cluster-lensed quasars are published in the literature, none has all the necessary time-delay measurements, space-resolution imaging, and spectroscopic redshifts of secondary arcs for a measurement of H_0. All four of the other published cluster-lensed quasars have ongoing photometric monitoring campaigns to measure their time delays. Additionally, one of the other four systems, COOL J0542-2125 (Martinez et al. 2023) will be observed by HST in Cycle 30 (GO-17243; PI: Napier).

To estimate the improvement in the H_0 constraint from a sample of twice as many time-delay measurements, we simulated H_0 distributions guided by the existing sample, as follows. We sampled integer H_0 values from a Gaussian distribution centered at our combined H_0 value of 74.1 km s^{-1} Mpc^{-1}. We then randomly assigned to these six H_0 values the standard deviation of one of the six H_0 distributions (Table 8), and produced the corresponding Gaussian distributions. We repeated this simulation process 100,000 times. Incorporating these new six H_0 distributions for a total of 12 constraints, and averaging the 100,000 iterations, gave a standard error of the weighted mean of 5.5 km s^{-1} Mpc^{-1}. Therefore, doubling the number of systems results in a ∼35%–40% improvement in the constraint on H_0, reducing the uncertainty on H_0 from 11% to ∼7.4%.

A 1% uncertainty measurement of H_0 from cluster-lensed quasars would be competitive with the current precision level of CMB and distance ladder methods. Extending the simulation described above to a larger number of systems, we estimated that 620 delay measurements from cluster-lensed quasars would achieve a 1% uncertainty level on H_0 from cluster-lensed quasars. Based on SDSS J1004+4112, SDSS J1029+2623, and SDSS J2222+2745 each having an average of two time-delay measurements, a sample size of 310 cluster-lensed quasars would be needed to produce 620 time-delay measurements. Future surveys are expected to detect of order ∼50 such systems in the next decade (Robertson et al. 2020). Therefore, this increase in sample size alone will not achieve a 1% uncertainty in H_0; to reach 1% with of order of 50 systems (100 time delays) will require a decrease in the lens modeling uncertainties by about a factor of two and a half, on average. Future work will explore whether this decrease in the uncertainties is feasible.

Acknowledgments

Based on observations made with the NASA/ESA Hubble Space Telescope, obtained from the Multimission Archive at the Space Telescope Science Institute (MAST) at the Space Telescope Science Institute, which is operated by the Association of Universities for Research in Astronomy, Incorporated, under NASA contract NAS5-26555. These archival observations are associated with programs GO-10509, GO-9744, GO-10793, GO-12195, and GO-13337. Support for HST program AR-16150, which enabled this work, was provided through grants from the STScI under NASA contract NAS5-26555. Coauthor G.M. received funding from the European Union's Horizon 2020 research and innovation program under the Marie Sklodowska-Curie grant agreement No. 896778. We thank Ana Acebron for her useful discussions about SDSS J1029+2623. We thank the anonymous referee for the constructive feedback and comments that improved the manuscript.

Facilities: HST(ACS), HST(WFC3), and HST(MAST).

Software: `Lenstool` (Jullo et al. 2007) and `Source Extractor` (Bertin & Arnouts 1996).

ORCID iDs

Kate Napier https://orcid.org/0000-0003-4470-1696
Keren Sharon https://orcid.org/0000-0002-7559-0864
Håkon Dahle https://orcid.org/0000-0003-2200-5606
Matthew Bayliss https://orcid.org/0000-0003-1074-4807
Michael D. Gladders https://orcid.org/0000-0003-1370-5010
Guillaume Mahler https://orcid.org/0000-0003-3266-2001
Jane R. Rigby https://orcid.org/0000-0002-7627-6551
Michael Florian https://orcid.org/0000-0001-5097-6755

References

Acebron, A., Grillo, C., Bergamini, P., et al. 2022, ApJ, 926, 86
Ali, S. S., Bremer, M. N., Phillipps, S., & De Propris, R. 2018, MNRAS, 480, 2236
Bayliss, M. B., Sharon, K., Acharyya, A., et al. 2017, ApJL, 845, L14
Bertin, E., & Arnouts, S. 1996, A&AS, 117, 393
Birrer, S., Millon, M., Sluse, D., et al. 2022, arXiv:2210.10833
Birrer, S., Shajib, A. J., Galan, A., et al. 2020, A&A, 643, A165
Birrer, S., & Treu, T. 2019, MNRAS, 489, 2097
Birrer, S., & Treu, T. 2021, A&A, 649, A61
Dahle, H., Gladders, M. D., Sharon, K., et al. 2013, ApJ, 773, 146
Dahle, H., Gladders, M. D., Sharon, K., Bayliss, M. B., & Rigby, J. R. 2015, ApJ, 813, 67
Dyrland, K. 2019, Master's thesis, Univ. of Oslo
Elíasdóttir, Á., Limousin, M., Richard, J., et al. 2007, arXiv:0710.5636
Fohlmeister, J., Kochanek, C. S., Falco, E. E., et al. 2007, ApJ, 662, 62
Fohlmeister, J., Kochanek, C. S., Falco, E. E., et al. 2013, ApJ, 764, 186
Fohlmeister, J., Kochanek, C. S., Falco, E. E., Morgan, C. W., & Wambsganss, J. 2008, ApJ, 676, 761

Forés-Toribio, R., Muñoz, J. A., Kochanek, C. S., & Mediavilla, E. 2022, ApJ, 937, 35
Freedman, W. L. 2021, ApJ, 919, 16
Gladders, M. D., & Yee, H. K. C. 2000, AJ, 120, 2148
Grillo, C., Rosati, P., Suyu, S. H., et al. 2020, ApJ, 898, 87
Hubble, E. 1929, PNAS, 15, 168
Inada, N., Oguri, M., Keeton, C. R., et al. 2005, PASJ, 57, L7
Inada, N., Oguri, M., Morokuma, T., et al. 2006, ApJ, 653, L97
Inada, N., Oguri, M., Pindor, B., et al. 2003, Natur, 426, 810
Johnson, T. L., & Sharon, K. 2016, ApJ, 832, 82
Jullo, E., Kneib, J.-P., Limousin, M., et al. 2007, NJPh, 9, 447
Klesman, A. J., & Sarajedini, V. L. 2012, MNRAS, 425, 1215
Kochanek, C. S. 2020, MNRAS, 493, 1725
Lemaître, G 1927, ASSB, 47, 49
Lemon, C., Anguita, T., Auger, M., et al. 2023, MNRAS, 520, 3305
Lemon, C. A., Auger, M. W., & McMahon, R. G. 2019, MNRAS, 483, 4242
Limousin, M., Kneib, J.-P., & Natarajan, P. 2005, MNRAS, 356, 309
Martinez, M. N., Napier, K. A., Cloonan, A. P., et al. 2023, ApJ, 946, 63
Moresco, M., Amati, L., Amendola, L., et al. 2022, LRR, 25, 6
Muñoz, J. A., Kochanek, C. S., Fohlmeister, J., et al. 2022, ApJ, 937, 7
Napier, K., Gladders, M. D., Sharon, K., et al. 2023, ApJL, 954, L38
Oguri, M. 2010, PASJ, 62, 1017
Oguri, M., Ofek, E. O., Inada, N., et al. 2008, ApJ, 676, L1
Oguri, M., Schrabback, T., Jullo, E., et al. 2013, MNRAS, 429, 482
Planck Collaboration, Aghanim, N., Akrami, Y., et al. 2020, A&A, 641, A6
Raney, C. A., Keeton, C. R., & Brennan, S. 2020, MNRAS, 492, 503
Refsdal, S. 1964, MNRAS, 128, 307
Riess, A. G., Yuan, W., Macri, L. M., et al. 2022, ApJL, 934, L7
Robertson, A., Smith, G. P., Massey, R., et al. 2020, MNRAS, 495, 3727
Ross, N. R., Assef, R. J., Kochanek, C. S., Falco, E., & Poindexter, S. D. 2009, ApJ, 702, 472
Schneider, P. 1985, A&A, 143, 413
Sharon, K. 2008, PhD thesis, Tel Aviv Univ.
Sharon, K., Bayliss, M. B., Dahle, H., et al. 2017, ApJ, 835, 5
Sharon, K., Chen, M. C., Mahler, G., Coe, D. & RELICS Collaboration 2023, ApJS, 264, 15
Sharon, K., Gal-Yam, A., Maoz, D., et al. 2010, ApJ, 718, 876
Sharon, K., Ofek, E. O., Smith, G. P., et al. 2005, ApJ, 629, L73
Shu, Y., Koposov, S. E., Evans, N. W., et al. 2019, MNRAS, 489, 4741
Shu, Y., Marques-Chaves, R., Evans, N. W., & Pérez-Fournon, I. 2018, MNRAS, 481, L136
Treu, T., Suyu, S. H., & Marshall, P. J. 2022, A&ARv, 30, 8
Wong, K. C., Suyu, S. H., Chen, G. C. F., et al. 2020, MNRAS, 498, 1420